Microstructural characterisation and in-situ straining of additive-manufactured X3NiCoMoTi 18-9-5 maraging steel

Ludmila Kučerová*, Ivana Zetková, Andrea Jandová, Martin Bystrianský

Regional Technological Institute, University of West Bohemia in Pilsen, Univerzitni 8, 30614 Pilsen, Czech Republic

ABSTRACT

Additive manufacturing (AM) is an advanced technology used for the manufacture of products that have intricate shapes and complex inner geometries. Various metal powders can be used for AM; however, the resulting microstructures will differ profoundly from those obtained via the casting, heat treatment, or thermomechanical processing of metals with the same chemical composition. This is because of the rapid heating and cooling rates used during three-dimensional (3D) printing. Further complications arise from the repeated heating and cooling of some regions, which is owed to the step-by-step formation of the solidified layers. A powder consisting of 1.2709 (X3NiCoMoTi 18-9-5) low-carbon maraging steel was used in an AM experiment. Given the high residual stresses that exist within printed metals, a post-processing heat treatment is desirable to limit the risk of cracking. In this study, solution annealing and hardening treatments were applied to the printed samples to induce changes in their microstructures and mechanical properties. The mechanical properties and microstructures of the builds were characterised and compared to those of a bar of conventional steel with the same chemical composition. During tensile loading, the fracture that was initiated at the sites of metallurgical defects was observed in situ.

1. Introduction

Maraging steels are high-strength steels with very low carbon contents, which are primarily alloyed with Ni, as well as Co, Mo, Ti, and Al. Following conventional annealing, the microstructure of such steels is fully martensitic, and they have very good machinability. Owing to the very low carbon content of these steels, and their high levels of Ni and other substitutional solutes, the martensite in these steels is considered to be a special, virtually carbon-free supersaturated solid solution of Ni (and some Co and Mo) in α-Fe. The final solid solution is relatively soft and ductile, with a typical hardness value of around 30 HRC. The high strength and hardness values are owed to the precipitation of inter-metallic phases, $Ni_3(Mo,Ti)$, during the final tempering process, which is performed at around 500 °C [1–3]. Maraging steels generally offer good resistance against deformation, excellent toughness, and homogeneous shrinkage (0.09%). Therefore, they are generally used in applications that demand reliability and excellent mechanical properties. They are used in the automotive industry, and are also used to manufacture tools with high surface strength and hardness, and dies used for injection moulding or pressure casting [1–8].

Currently, maraging steels can be processed via conventional casting, forging, heat treatments, and additive manufacturing (AM). In general, AM is a term used to describe a range of rapid prototyping methods that are based on the layer-by-layer deposition of the material of the final product. The materials that can be processed by these technologies range from plastics and plastic-based composites, to metals. The feedstock can be in the form of a liquid or solid state; they include powders, fibres, and thin plates. Selective Laser Melting (SLM) is an advanced AM technique; it uses the powder-bed fusion technique, and is also known as Direct Metal Laser Sintering (DMLS) [1–3]. Here, three-dimensional (3D) computer models of final parts are split into many parallel layers. The geometry and thickness of these layers govern the formation of the individual physical layers of a molten material. A laser beam is traversed above the powder bed, and melts the powder layers. The beam produces layers with thicknesses of 20–100 μm [1–5]. The working space is usually purged with inert gas to prevent oxidation. SLM can be used to produce parts with relatively complex outer and inner geometries because the laser beam can be programmed to melt precisely defined areas in each layer. For instance, tool inserts intended for polymer-injection moulding, in which the inner cooling channels are very close to the working surfaces, can be manufactured. This offers very efficient cooling of the injected polymer. However, the surface quality of the resultant products is still substandard and some post-processing is often necessary. This involves removal of the

supporting structures and occasionally, detachment of powder grains that remain attached to the surface. The rapid in-process heating and cooling of the build results in high residual stresses within the product [4]. These stresses are more severe in large or complex-shaped products, which are prone to distortion or even cracking. To relieve these stresses, various heat treatments are applied immediately after the SLM process. In addition, such post-processing heat treatments can favourably alter the mechanical properties of the product. For instance, the product strength can be increased significantly via the application of an appropriate precipitation-hardening treatment [4–6].

As mentioned above, the laser processing of metals involves high heating and cooling rates (typically around 10^6 K/s), which result from short interaction times and high thermal gradients [7,8]. These rapid changes in temperature often lead to very unusual, non-equilibrium microstructures, including new phases with extended composition ranges [7,8]. Therefore, AM microstructures differ from those of non-AM materials with an identical composition that received a conventional heat treatment [7,9]. Following such rapid cooling, the resultant microstructures may be expected to consist solely of a martensitic matrix that is free from precipitates and retained austenite. Powder tool steels obtained via AM processing are reported to possess unusual microstructures; initial studies have [1,2] demonstrated that these microstructures are more comparable to those of maraging steels produced by laser welding or surface treatments [7,9] than those of conventional, cast tool steels. Several researchers have studied the microstructures of powder steels following surface-laser treatments [10–12] and have characterised the powders used for AM [13–17]. There are relatively few studies that have focused on the unique microstructures of AM-processed and heat-treated powder tool steels [1,4,7–9]. The findings reported for 18Ni-300 maraging steel are not always unanimous. Recently, researchers have attempted to identify the precipitates within AM maraging steels and have studied the effects of heat treatment on their microstructural evolution [7,8]. Some authors have claimed that no precipitation was detected in post-SLM 18Ni-300 maraging steel [1,18]. It is difficult to compare the microstructures reported by various authors because the effect of etching on the appearance of AM microstructures has been largely ignored. This article will demonstrate that the use of unsuitable etchants can result in the loss of information that could be of importance when evaluating the influence of AM parameters on the microstructure. SLM results in materials with completely different microstructures to those that are conventionally processed. However, the static mechanical properties of SLM-processed materials are similar to, or better than conventionally processed materials of an identical chemical composition. However, AM also results in particular defects, which can critically affect the mechanical behaviour of the steel. The in-situ observation of the failure initiation and propagation, owed to such defects, under tensile loading will be described in this article.

2. Experimental programme

2.1. Material

This work focuses on the microstructural analysis of a maraging powder tool steel, X3NiCoMoTi 18-9-5, which is equivalent to 1.2709. This steel is also available under the name MS1. The powder was obtained from EOS GmbH, which is the supplier of the EOS M290 printing machine that uses the SLM method. The X3NiCoMoTi 18-9-5 maraging steel can also be purchased in the form of conventionally produced bars, under the commercial name Vaco 180.

The powder was produced by gas atomization, which is one of the most common powder-steel production methods. Atomization typically generates relatively regularly shaped, spherical particles. During the process, the metal alloy is melted, and the molten stream is disturbed by a high-velocity gas stream. This breaks the liquid metal into fine droplets, which then solidify as individual powder grains. Table 1

2.2. Additive manufacturing and heat treatment

The AM process was performed within the EOS M290 machine using parameters recommended for tool steels, namely a laser power of 258 W, scanning rate of 960 m/s, and layer thickness of 40 μm. A protective atmosphere of nitrogen gas was used to prevent oxidation during the AM process. A subsequent heat treatment was performed under an argon atmosphere. Unless stated otherwise, the micrographs below show the cores of the builds, where the angle between the laser tracks within the consecutive layers is 67°. The contour (skin) of the build, which was produced by a laser beam that travelled in only one direction, is documented to compare the visibility of the laser tracks revealed by various etchants.

The rapid heating and cooling of the powder layers results in steep thermal gradients, which consequently result in the generation of high residual stresses within the builds. To eliminate the risk of cracking, solution annealing was performed on some builds. The annealing was performed at 820 °C for 20 min. This was followed by rapid cooling to a temperature below 500 °C. Subsequently, the material was cooled to room temperature within the furnace (Fig. 1).

In addition, some other builds were precipitation hardened to increase their hardness and strength. They were held at 490 °C for 6 h, and then slowly cooled to room temperature (Fig. 2).

2.3. Microstructural characterisation

The powder was examined using scanning electron microscopy (SEM). Random samples of loose particles were placed on conductive glue tape, which was used to cover a stub. The samples were observed using a Zeiss EVO 25 scanning electron microscope (SEM) with a LaB_6 cathode. Image analysis was performed at a magnification of $1000 \times$ to evaluate the average particle size and particle distribution. Customised software, 'Zrno', was used to measure the particle diameters. Metallographic cross-sections of the particles were prepared to characterize their microstructures and local chemical compositions using energy-dispersive X-ray spectroscopy (EDS, Oxford Instruments). The microhardness of the cross-section of the particles was measured using a UHL VMH-002V hardness tester.

Builds, in three states, were obtained using different processing sequences. As-built samples, annealed samples, and hardened samples were obtained. Detailed metallographic examination was performed on the samples using SEM and electron back scattered diffraction (EBSD) analysis; the local chemical composition of each sample was also characterised. The microstructures of two perpendicular cross-sections were observed for each sample. A side cross-section was prepared along the building direction, whereas a top cross-section was prepared parallel to the hatching planes. A dual-beam SEM (Auriga) was employed, which had a focused-ion beam (FIB), an EDS detector, EBSD detector, and a field emission gun (FEG) electron source. The samples intended for microstructural observation were etched with 3% nital, Adler's reagent, Fry's reagent, and dilute aqua regia (H_2O:HNO_3:HCl = 6:1:3). Unetched samples, polished with colloidal silica, were documented for comparison. Samples for EBSD analysis were prepared via conventional mechanical polishing with colloidal silica, and electrolytic polishing, to obtain a deformation-free surface. The final electrolytic polishing was conducted at room temperature in a mixture consisting of 500 ml of ethanol, 25 ml of 60% $HClO_4$, and 7.5 ml of HNO_3, using a voltage of 31 V, flow rate of 14, and polishing time of 10 s.

The porosity levels of the printed samples were evaluated via optical microscopy and subsequent image analysis of the polished surface. The measurements were conducted on the side and top cross-sections. On each cross-section, the area ratio of the pores was evaluated using stitched images of a surface area measuring 1×1 cm. The majority of the pores were relatively circular in shape; therefore, the difference between the results obtained for the side and top cross-sections was negligible, and an average value is discussed in the text.

Table 1
Chemical composition of the powder, in wt%, as stated by EOS GmbH.

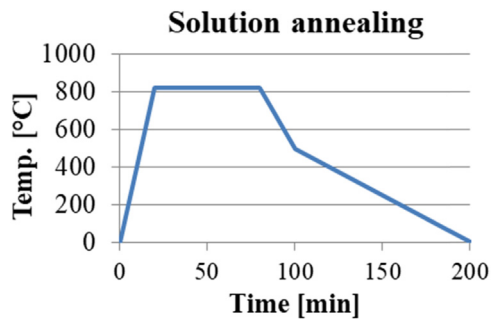| C	Si	Mn	Cr	Ni	Mo	Nb	Ti	Co	Al
≤0.03	≤0.1	≤0.1	≤0.5	17–19	4.5–5.2	–	0.6–0.8	8.5–9.5	0.05–0.15

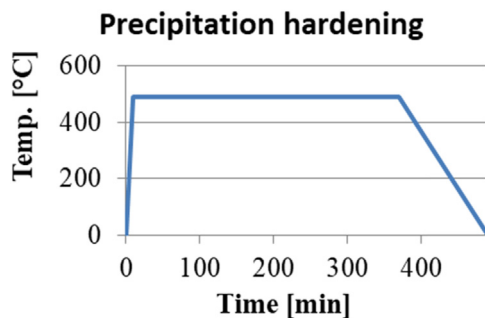Fig. 1. Solution annealing performed to relieve residual stresses.

Fig. 2. Precipitation-hardening treatment.

Fig. 3. In-situ testing stage.

Fig. 4. Dimensions of the tensile samples.

The phase fractions were determined via X-ray diffraction using an automatic powder diffractometer (AXS Bruker D8 Discover) with a HI-STAR detector and Co lamp ($\lambda K\alpha$ = 0.1790307 nm). A focusing poly-capillary lens was used to achieve an X-ray spot with a 0.5-mm diameter. The measurement was conducted in the central regions of the builds. Spectra were recorded over the 2ϑ range of 25–110°. The integrated intensities of the (200) ferrite peak and (111), (002), and (022) austenite peaks were used to evaluate the volume fractions of the ferrite and retained austenite.

2.4. Mechanical testing

The mechanical properties of the samples were determined by tensile and hardness testing. A hardness tester (UHL VMH-002V) with a Vickers indenter and load of 100 g was employed. Five indents were randomly placed in the centre of every sample. The average hardness was calculated for every material state.

Tensile tests were performed on a deformation stage (Fullam MTI II deformation stage) (Fig. 3) using flat, dog-bone-shaped samples with a gauge length of 15 mm and a cross-section of 1.5 × 1.2 mm (Fig. 4). The dimensions of the sample were based on standard EN ISO 6892; the total length was based on criteria related to the testing stage. A proportional, flat sample, with a proportionality coefficient of 11.3, was used, which is recommended for samples with small cross-sections. The samples were printed in three key directions, namely X, Y, and Z. Directions X and Y lie in the platform plane, whereas Z corresponds to the building direction, which is perpendicular to the platform. For each material state (as-built, annealed, hardened), three samples were tested for each direction. Continuous tensile loading was employed to determine the yield strength, ultimate tensile strength, and total elongation of each sample. The average value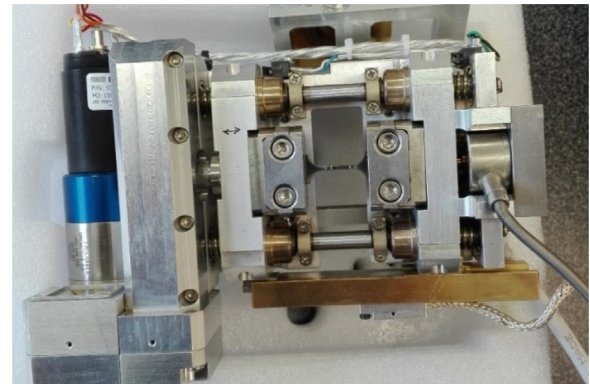s of the yield strength, ultimate strength, and total elongation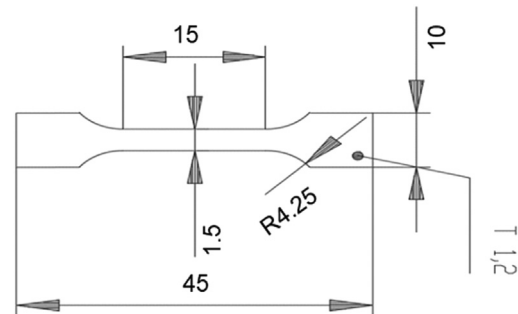 were evaluated for every material state, regardless of the printing direction. The effects of the printing direction on the mechanical properties have been reported elsewhere [19].

For comparison, samples of the same geometry were manufactured from conventional maraging steel of the same chemical composition, Vaco 180, which were subjected to identical heat treatments. For each heat-treated state, three samples were tested in tension. The average values of the results are reported. The hardness values (HV 0.1) of these samples were also measured.

2.5. In-situ testing

The Fullam MTI II deformation stage (Fig. 3) was also used for in-situ deformation experiments, where flat, dog-bone shaped samples, identical to those used for tensile testing (Fig. 4), were tested in the as-built condition. These samples were printed in one direction, with the sample axis parallel to the platform surface. The surfaces of these samples were prepared in the form of metallographic sections; the samples were ground and polished and the final polishing was performed using colloidal silica. The samples were glued to larger blocks, and subsequently, they were manually ground and polished to ensure a constant thickness and a scratch-free surface. The polished surfaces were etched with 3% nital to reveal the microstructure.
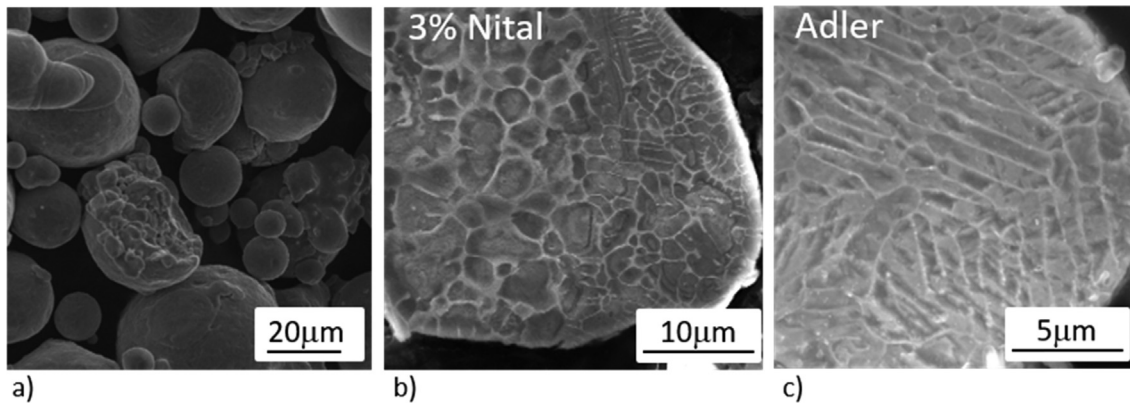
Fig. 5. (a) General view of powder particles. Cross-sections of the particles etched with (b) nital; and (c) Adler's reagent.

3. Results and discussion

3.1. Characterisation of powder

The powder particles had various shapes (Fig. 5). In general, they were either spherical or highly-elongated; occasionally, they possessed an indeterminate shape that resembled the jagged fragments of crushed particles. Spherical particles, with a wide range of sizes, were most frequently observed. Some particles were very fine, with diameters of several micrometres. Others were large, with several satellites (fine, globular particles) attached to them. These conglomerates, consisting of large particles with satellites, are often found in gas-atomized powders [13].

The average size of the particles and their size distribution were determined by image analysis. The average particle size was 24.8 μm. Approximately 60% of the particles had sizes of 20–30 μm. It is important to determine the actual size distribution of the powder particles to ensure reliable AM production quality. Considering workplaces that utilise such powders, this information can also be used to determine the use of appropriate safety measures and personal protective equipment.

All the particle types exhibited a dendritic or cell morphology (Fig. 5a), which was confirmed by the observation of the metallographic cross-sections (Fig. 5b and c). Measurement of the local chemical compositions revealed the existence of Fe-based inclusions within the powder grains. In addition, the alloying elements were not distributed uniformly; the boundaries of the cells and dendrites contained

greater quantities of Mo, Ni, and Ti than the matrix (Fig. 6).

The microhardness of individual particles was measured. Based on the results obtained for ten particles, the average microhardness value was determined to be 336 HV 0.01. The readings were within the range of 286–357 HV 0.01.

3.2. Microstructural analysis of the printed samples

3.2.1. As-built state

When the polished surfaces were viewed under a light microscope, very few pores were observed; this is because the overall porosity of the builds was below 1%. Laser tracks (i.e., melt-pool boundaries), which cross at an angle of 67°, can be observed on the top cross-section (Fig. 7a–c). The images of the side cross-sections show sections of the tracks (Fig. 7d–f). Under the light microscope, the microstructure appeared to be lamellar because its actual cellular nature was impossible to discern using optical microscopy. It should be noted that each etchant revealed significantly different microstructural features. Fig. 8 shows the same locations of the sample following etching with 3% nital (Fig. 8a) and Adler's reagent (Fig. 8b and c). The microstructures that could be observed with the use of Adler's etch resembled the conventional microstructures of cast maraging steels. This etchant barely revealed traces of the 3D-printing process because it highlighted martensite packets. The nital etch predominantly revealed laser tracks and details of the cellular microstructure, but did not reveal any signs of typical martensite features (Fig. 8a). This is because nital preferentially
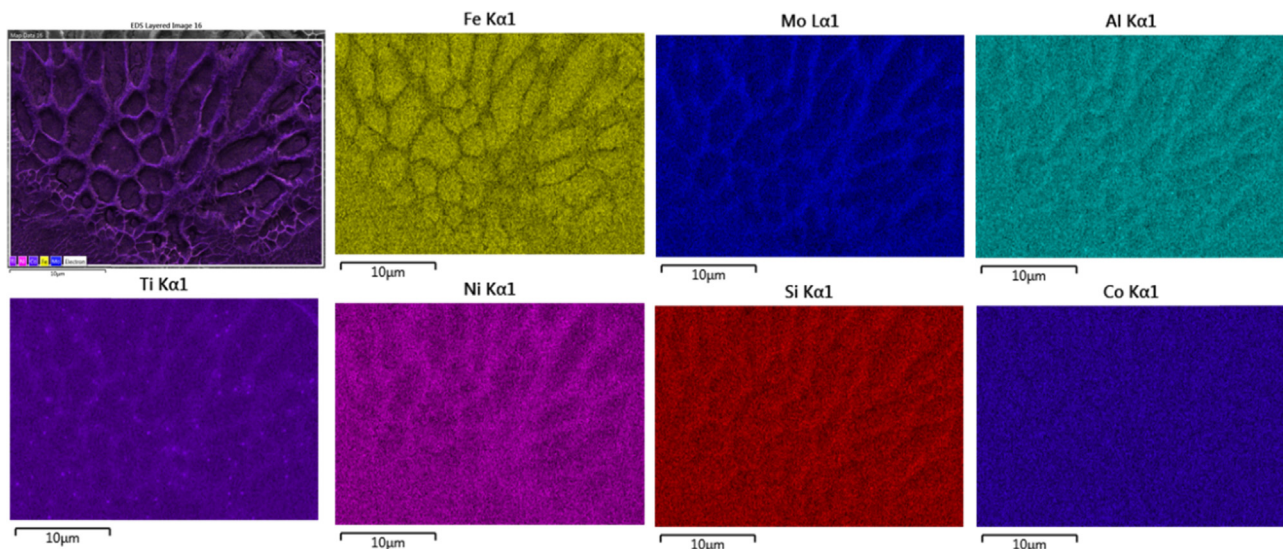

Fig. 6. Distribution of the alloying elements within a powder particle.
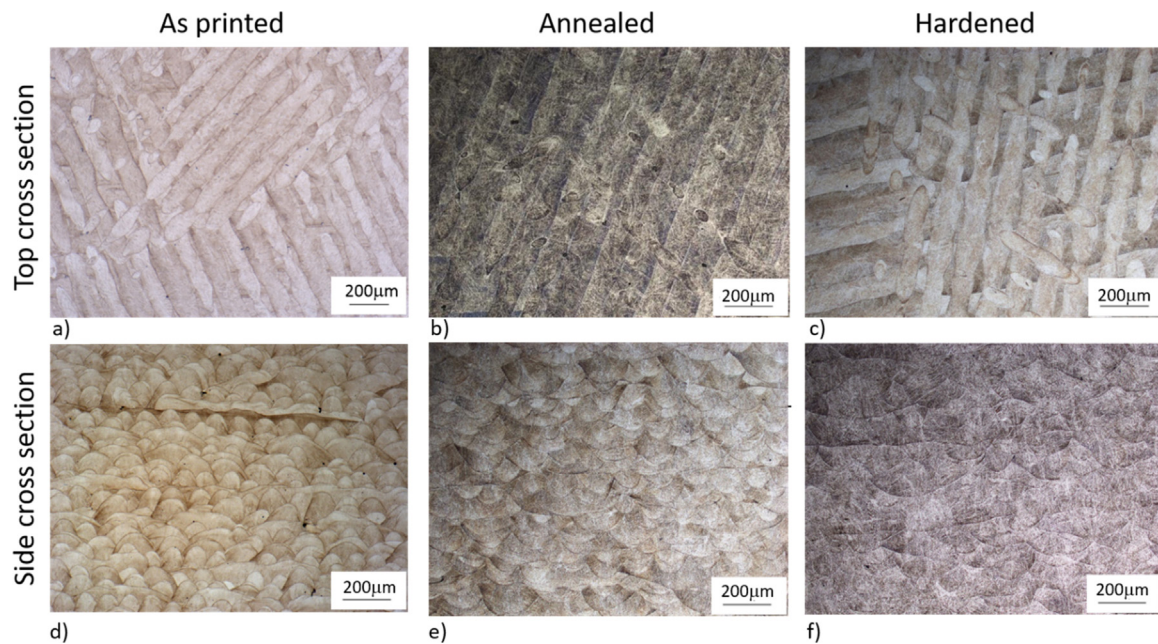
Fig. 7. Light micrographs of two perpendicular cross-sections of the samples, which were etched with 3% nital. The top cross-sections of the (a) as-printed sample; (b) annealed sample; and (c) hardened sample, and side cross-sections of the (d) as-printed sample; (e) annealed sample; and (f) hardened sample.

attacks alloy-rich segregations and clearly highlights the solidification substructure [4]. The areas that were etched with Adler's reagent appear to be similar to those shown in the EBSD images, which had a similar crystallographic orientation; however, in the SEM micrographs, a fine cellular microstructure can also be distinguished within the martensitic laths.

It is thus important to consider the purpose of the microstructural analysis, and select an appropriate etching method. As shown in Fig. 8b, any evidence of the 3D-printing process was completely absent when Adler's etch was used. The micrographs shown in Fig. 8a and b show a surface of a printed sample, where the printing conditions were slightly altered for the contour layer. In the case of the cross-section that was etched with nital (Fig. 8a), a clearly visible surface layer can be observed. However, this is completely indistinguishable in the case of the cross-section that was etched with Adler's etch (Fig. 8b and c).

The microstructure was cellular with two types of cell morphologies, namely equiaxed and substantially columnar (Fig. 9a and b). Following conventional heat treatment, the cellular solidification morphology is not commonly found in maraging steels because it results from the very high heating and cooling rates that are used during 3D printing; the rapid solidification prevents the formation of conventional lath martensite [1].

Regardless of the cell shape, the matrix consisted of a single solid

solution, with the cell boundaries lined by a second phase. Coarse particles were primarily observed at the cell boundaries and triple points. However, a few coarse particles and many fine particles were also dispersed within the cells. The distribution of the alloying elements was identical for both types of cells. The cell boundaries were comparatively richer in alloying elements (Ni (21%), Mo (5%), and, locally, Ti). This is generally attributed to the occurrence of micro-segregation during solidification, i.e., the partitioning of these elements into the remaining liquid during solidification [1,7,18]. It is interesting to note that the heterogeneous distribution of the alloying elements corresponds to the alloy distribution of the powder particles shown in Fig. 6.

The chemical analysis of the particles showed that they contained the majority of the Ti present in the steel. Compared with the matrix, they were also richer in other alloying elements, particularly Mo. This corresponds with the reported presence of Ni_3Ti particles in AM maraging steels [6,7]. The Ti in these precipitates is also often partially or fully substituted with Mo or Al. The presence of other alloying elements within these fine Ti-rich precipitates indicates that they are not Ti oxides resulting from insufficient protection by the inert gas during the AM process, as suggested by previous researchers [18].

Equiaxed cells of various sizes could be observed. Relatively large areas, consisting of cells with similar geometries, could be observed, which were visibly separated from other areas consisting of cells with
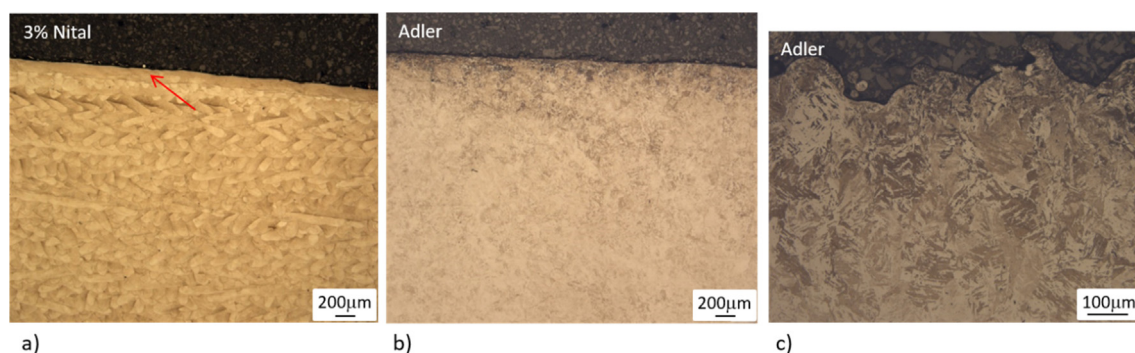

Fig. 8. (a) Surface of a printed sample that was etched with 3% nital; the contour layer (indicated by an arrow) is only visible in this case. (b, c) Detail of the microstructure of the surface region, which was etched using Adler's etch.
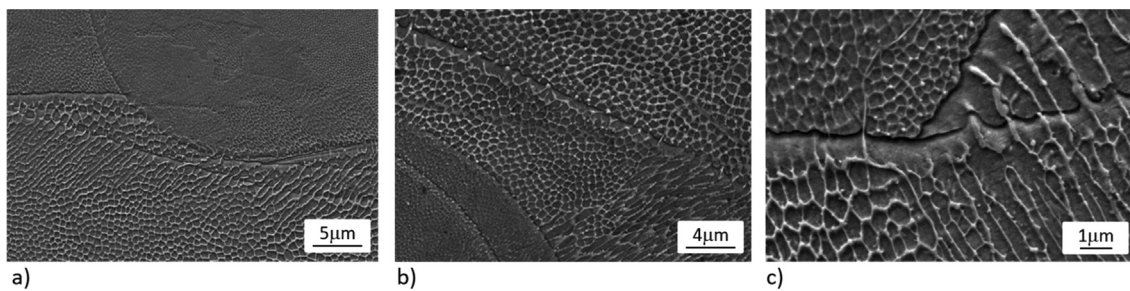
Fig. 9. SEM micrographs of the as-built samples, etched using 3% nital. (a), (b) areas with different cell morphologies; (c) epitaxial growth.

differing cell sizes or morphologies. In several locations, epitaxial growth of the cells into neighbouring areas was observed (Fig. 9c). Similar effects were reported in other studies on powder maraging steels with martensitic microstructures; this suggests that the composition gradient does not affect the development of the martensite blocks, and that the growth of martensite is not constrained by the cell boundaries [4,5].

Areas with various morphologies and cell sizes were occasionally observed within a single laser track. The columnar cells had a length of 2–15 μm and width of approximately 1 μm. The equiaxed cells were much finer, with a typical size of approximately 1 μm or smaller. Other researchers have reported the observation of cellular microstructures, with an intercellular spacing of around 1 μm, in maraging steels [1,6,7]. The good strength and hardness of this steel is assumed to due to this fine, cellular structure [1,8].

Similar results were obtained during the electron-probe analysis of 1.2709 steel. Here, the Mo and Ti within the inter-cellular spaces were substantially segregated during solidification. However, the segregation of Ni and Co was less pronounced [4].

Based on the X-ray diffraction analysis, the volume fraction of the retained austenite was about 4%. Its lattice parameter was 0.36034 nm. Although retained austenite is rarely found in conventional maraging steels, its presence in AM steels is quite common, as reported by Kempen et al. [1] and others [7,10,18]. Using X-ray diffraction, Kempen et al. [1] found that an as-built SLM part, consisting of 1.2709 steel, had an austenite volume fraction of approximately 6%. In this particular work, the X-ray diffraction analysis did not generate any information on the distribution of the retained austenite. However, in previous studies, the 'reversed austenite' was also stabilized in the inter-dendritic areas of laser-treated weld fusion zones that had increased contents of Ni [16] and other solutes [10].

3.2.2. Solution-annealed state

A previous report [7] states that in the case of such maraging steels, any traces of the solidification process vanish completely following a solutioning heat treatment; however, in the case of the present builds, which were etched with nital, very little difference was found between the light micrographs of the as-built and solution-annealed microstructures (Fig. 7). The aforementioned report may have been based on the observation of sections etched with Adler's reagent. This is because, in the case of the present specimen, this etchant revealed very different microstructures with obscured laser-beam tracks (Fig. 10a). Fry's reagent is sometimes used to etch 3D-printed maraging steel [10]. In this study, it revealed some laser tracks, although less clearly than nital (Fig. 10b). Another etchant, aqua regia, which is used to etch AM maraging steels [4], also revealed some traces of the laser-beam tracks (Fig. 10c).

The detailed SEM observation showed that the original cells had disappeared, and that in addition to Ni_3Ti and $Ni_3(Ti, Mo)$, a new type of Co-rich particle became visible (Fig. 11). The X-ray diffraction analysis did not reveal any retained austenite within the annealed microstructure. This is consistent with the reversion of the original retained austenite during heating and annealing, as reported by previous studies

[7,8]. Nital preferentially attacked the matrix around numerous particles, or their groups, creating patterns with a regular dimple-like morphology (Fig. 11). This selective etching revealed a large quantity of predominantly globular particles of various sizes within the matrix. The grain boundaries were more visible under the backscattered electron (BSE) mode (Fig. 11b). Fry's reagent seemed to be unsuitable for observation under high magnifications. This is because it created characteristic etching reliefs that were very deep, which obscured the actual microstructural features. Adler's reagent also tends to result in certain etching reliefs, even following very mild etching. These reliefs resemble the original cell microstructure of the as-built sample (Fig. 12a). Simultaneously, the shape of the martensite laths was clearly visible. Following final polishing with colloidal silica (OP-S, Struers), interesting micrographs were obtained without etching, under the BSE mode (Fig. 12b). This technique revealed a very fine microstructure consisting of fine, slightly elongated areas that were coloured various shades of grey. This resembled the lath-like pattern of the dimple-like morphology of the nital-etched sections. However, based on these images, it was difficult to evaluate the development of the annealed microstructure, and compare it to microstructure of the as-built specimens. The most satisfactory results were obtained when aqua regia was used as an etchant (Fig. 12c). In contrast to the nital etch, the matrix around the particles was not selectively attacked, and sufficient relief was obtained to evaluate the microstructural development.

3.2.3. Precipitation-hardened state

The precipitation-hardening treatment at 490 °C caused most of the original cell microstructure to dissolve. Uneven etching was not encountered with 3% nital, and therefore no other etchants were tested. Scattered, elongated islands, consisting of a white-coloured phase, remained at the prior cell boundaries (Fig. 13a and b). The laser tracks remained visible in the light micrographs (Fig. 7). The X-ray diffraction analysis detected retained austenite at a volume fraction of 8%. This is double the amount of that in the as-built steel. The lattice parameter was $a = 0.35991$ nm, which corresponds well with the lattice parameter of the as-built sample. In addition, Ni_3Ti and $Ni_3(Ti, Al)$ particles were found in the microstructure. As shown in the high-magnification images, extremely fine particles were dispersed in the matrix (Fig. 13c). Nanoprecipitation of these particles during hardening was confirmed by Tan et al. [7], who performed a high-resolution transmission electron microscopy (HRTEM) study on this steel. Coarse particles, which were frequently present in the as-built and annealed samples, were rarely found in the precipitation-hardened samples.

3.2.4. EBSD analysis

The matrix of the as-built material comprised a BCC lattice (Fig. 14a). In addition, FCC austenite, at a volume fraction of just over 2%, was identified at the cell boundaries by EBSD. This was equal to half of the average volume fraction of the retained austenite, as determined by X-ray diffraction. Even though austenite was only detected in some parts of the cell boundaries, it seems reasonable to assume that a larger portion of the phase that lined the cell boundaries was indeed austenite. This phase exhibited the form of a thin film, with a typical
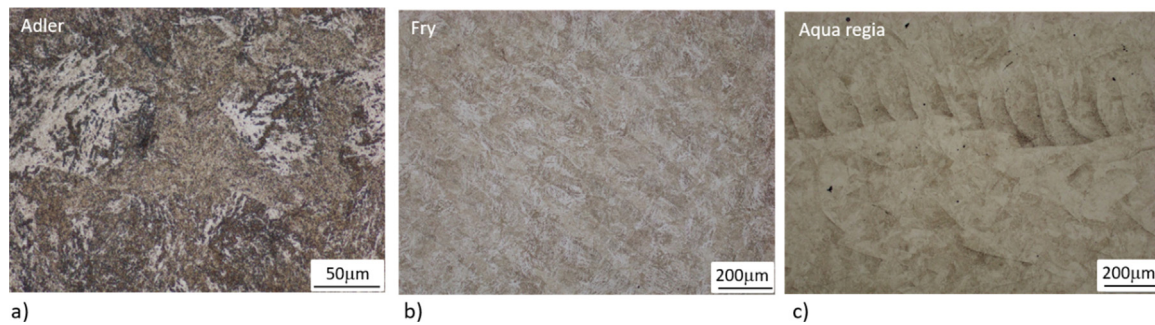
Fig. 10. Top cross-section of the annealed material, etched with (a) Adler's reagent; (b) Fry's reagent; and (c) Aqua regia.

thickness of several hundred nm; therefore, it may be difficult to evaluate because of issues related to the EBSD resolution. The difference between the X-ray diffraction and EBSD results could also be attributed to the variation in the retained-austenite distribution. This is because significantly smaller areas were determined by EBSD. It was previously reported [18] that retained austenite is more likely to be found in the vicinity of melt-pool boundaries. The exclusive presence of retained austenite at the cell or dendrite boundaries has also been documented by other studies on AM maraging steels. It is expected that the relatively high alloying-element contents of these areas will support the stabilization of austenite [8,19]. For the area under analysis, inverse pole figures (IPFs) were obtained in the direction of the laser tracks (Y) (Fig. 14d), and along the building direction (Z) (Fig. 14g). The groups of neighbouring cells exhibit identical or very similar orientations; however, the areas near the cell boundaries, identified as FCC austenite, have their own common orientation.

The microstructure of the solution-annealed sample consisted of numerous areas that primarily consisted of fine, elongated cells (Fig. 14b, e, and h). No retained austenite was detected, which correlates with the results of the X-ray diffraction phase analysis (Fig. 14b). This also corresponds with results published by other researchers. In comparison with the as-built sample, there was a larger variety of crystallographic misorientations between neighbouring areas (Fig. 14e and h).

Using EBSD, retained austenite, with a volume fraction of 1.5–6%, was detected in various analysed areas of the precipitation-hardened sample (Fig. 14c). The retained-austenite particles were fine, and often elongated in the directions perpendicular to the boundaries between areas of the matrix with different crystallographic orientations. The EBSD analysis determined that the fine, elongated islands (white-coloured areas in Fig. 13) consisted of austenite. It also confirmed that the precipitation-hardened sample contained more retained austenite than the as-built sample. A reverse reaction is expected to occur within this steel at hardening temperatures, which will generally lead to an increase in the retained-austenite volume fraction. This was observed in the case of 3D-printed samples, as well as in conventional precipitation-hardened samples of the same steel [5,7,18].

As shown by the IPFs obtained for the scanning plane (IPF Y, Fig. 14f), the crystallographic orientations of the retained-austenite grains of the as-built and hardened samples differ from that of the matrix. This difference was less pronounced along the building direction (IPF Z, Fig. 14i) of the as-built sample, but still significant in the case of the precipitation-hardened sample.

3.3. Mechanical properties

The maximum microhardness value of the as-built steel was 371 HV 0.1 (Table 2). Following solution annealing, it decreased to 328 HV 0.1 owing to the release of residual stresses caused by the high cooling rates used during the AM process. The dissolution of the fine, cellular microstructure also contributed to this reduction. The precipitation hardening resulted in a significant, almost two-fold increase, in the microhardness, to 665 HV 0.1. This was caused by the extensive precipitation of fine Ni_3X particles. These hardness values are slightly higher than those specified by the powder supplier; the hardness of the as-printed material is 327–363 HV and that of the post-precipitation-hardened material is 513–612 HV. Following solution annealing, the hardness of our sample is identical to that reported by the powder supplier for the post-printed material. Following corresponding heat treatments, the microhardness of an equivalent conventional maraging steel exhibited the same trends. The as-printed AM steel had a greater hardness than the equivalent conventional steel; this could be attributed to the very fine, cellular microstructure of the AM steel.

The stress-strain curves obtained for all three states are plotted in Fig. 15. They show that the annealed samples had slightly greater elongation and lower strength values than those of the as-built samples. The precipitation hardening caused a significant increase in the tensile strength. The average tensile properties are listed in Table 2, along with those of an equivalent conventional steel, Vaco 180. The mechanical properties of the printed samples were based on the average values of the results obtained for the samples printed in directions X, Y, and Z. A detailed analysis of the effects of the printing conditions on the mechanical properties has been given elsewhere [18]. Following identical treatments, the strength properties of the AM steel match or surpass
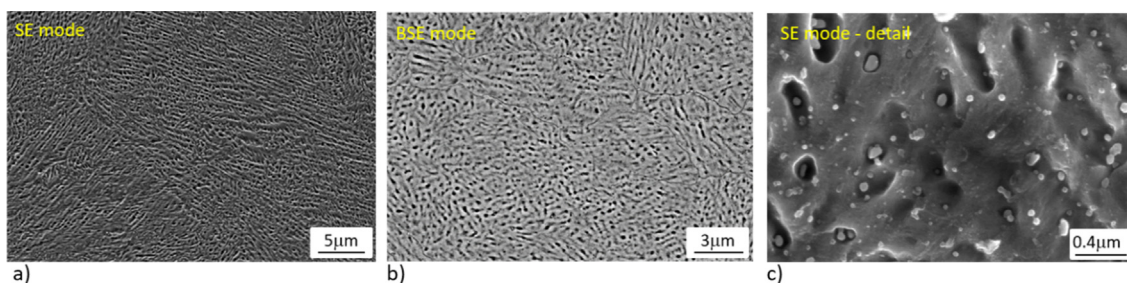

Fig. 11. Top cross-section of the annealed material, etched with 3% nital, revealed in (a) SE mode; and (b) BSE mode. (c) Numerous particles of various sizes, with mainly globular shapes, are embedded in the matrix. However, the areas of the matrix that are in close proximity to larger particles (or groups of particles) are preferentially etched away, creating a typical pattern with deep dimples.
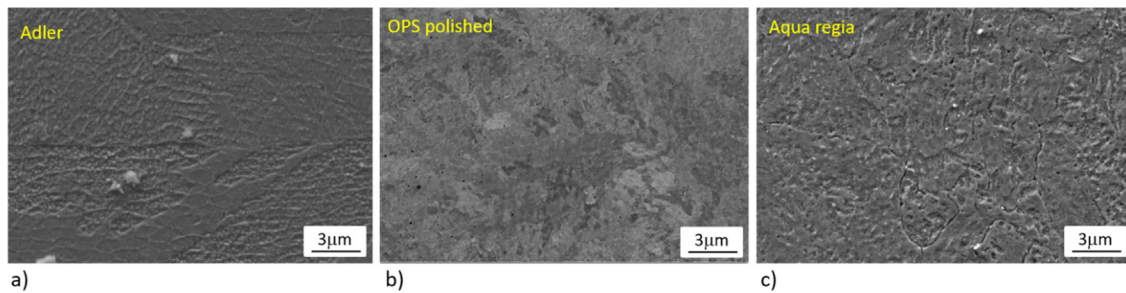
Fig. 12. Microstructures of the top cross-section of the annealed material. (a) Etched with Adler's reagent; (b) A polished unetched sample; (c) Etched with aqua regia.

those of the conventional steel. However, the total elongation values of the AM samples were always lower than those of the conventional steel. The residual stresses within the as-built material were relieved by the solution-annealing treatment; this resulted in a small decrease in the tensile strength and an increase in the total elongation. The precipitation hardening resulted in the production of many very fine precipitates, which were uniformly distributed in the matrix. These particles resulted in the pinning of dislocations, which consequently resulted in significant strengthening of the steel.

3.4. Fractography

The fracture surfaces of three samples, representing each material state, were documented (Fig. 16). The as-built and annealed samples exhibited typical ductile cup-and-cone-type fractures with large shear lips and extensive necking regions (Fig. 16a and b). The fracture surfaces displayed a typical dimple-like morphology, with many dimples of various sizes (Fig. 16d and e). Two relatively large holes were observed near the centre of the as-built sample (Fig. 16a). Some dimples originated at the sites of prior defects, and served as crack-initiation sites, similar to those observed during the in-situ testing. Fine holes were observed at the bases of larger dimples, which suggests that micro-voids had formed and coalesced. Elongated dimples were observed around large holes that were present within the central portion of the specimen, suggesting that the deformation direction was consistent.

The macroscopic image of the fracture surface of the annealed sample (Fig. 16b) is similar to that of the as-built sample. Ductile fracture occurred in the annealed sample, and a dimple-like morphology was observed. Dimples of various sizes were observed; there was a greater proportion of larger (broader) dimples, which often had a number of finer dimples at their base (Fig. 16e).

Compared with the other samples, the fracture surface of the hardened sample appeared to be more brittle with less elongation or necking (Fig. 16c). The fracture surface was more planar with several secondary cracks, and no shear lips. Compared with the previous two cases, there were significantly fewer dimples present. The areas between the dimples either contained many small, flat facets or many small dimples that were very shallow (Fig. 16f). This indicates that

quasi-cleavage was the main fracture mechanism in the case of the precipitation-hardened samples.

3.5. In-situ observation

The sample, on which in-situ testing was eventually performed, was first examined to identify potential fracture-initiation sites. These sites were then monitored during straining. Several defects were found in the gauge section of the sample (Fig. 17). They included cavities, pores, Fe- and Ti-based inclusions, and an unmelted particle.

The surface of this flat, dog-bone-shaped sample was ground, polished, and etched with 3% nital to the same quality standard as that of the standard metallographic cross-sections (Fig. 18d). It was then mounted in the test stage. The central portion of the sample was examined to identify areas of interest, such as potential failure-initiation sites. It was challenging to identify sites of this kind prior to the actual loading. In fact, it was necessary to perform several tests on these samples to obtain sufficient information to select appropriate locations for observation and documentation. High magnifications (× several thousand) were necessary to reveal the microstructural features, and this severely reduced the size of the area observed. The coordinates of the areas of interest were recorded in the control software to enable rapid, repeated documentation during the loading experiment. The aforementioned sample was then subjected to discontinuous tensile loading within the chamber of a SEM. The straining was interrupted ten times to capture micrographs of five areas of interest (Fig. 18e). These interruptions were planned based on the mechanical-property results and stress–strain curves obtained from previous continuous-loading tests. The area of plastic deformation was specifically observed during the test. The impact of the printing defects on the mechanical behaviour of the sample was directly observed. In the case of the as-built sample shown in Fig. 18, the behaviour around two defects (Fig. 18a and g) was observed. Both defects were located relatively close to the edges of the sample; the defect shown in the top row of images (Fig. 18a, b, and c) was located at a distance of approximately 200 μm from the edge of the sample. The defect shown in the bottom row of images (Fig. 18g, h, and i) was located at a distance of 50 μm from the edge of the sample. Both defects protruded into the core microstructure of the printed sample.
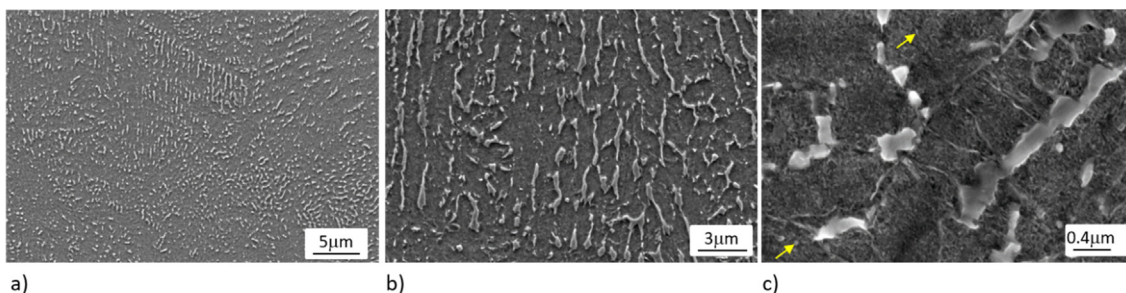

Fig. 13. Top cross-section of the precipitation-hardened microstructure. (a) Secondary phase (bright particles); (b) detail of the secondary phase observed at the prior cell boundaries; (c) High-resolution micrographs showing details of extremely fine particles (indicated by arrows).
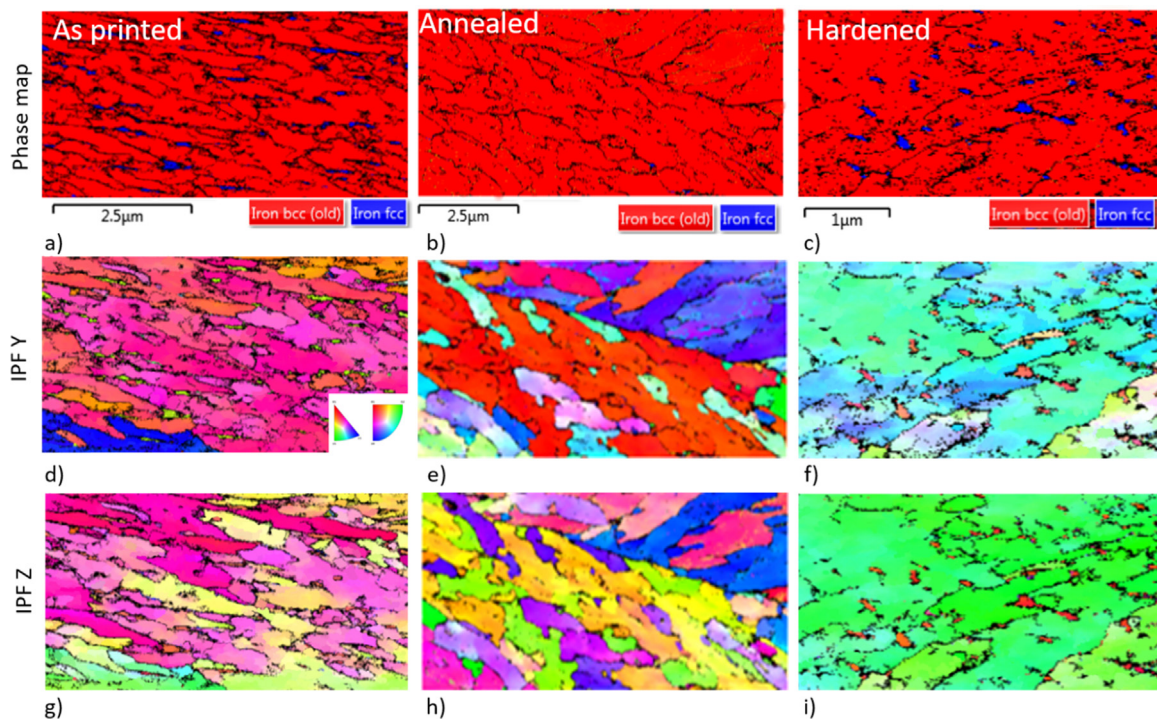
Fig. 14. Phase maps showing the distribution of the retained austenite (blue) within the (a) as-printed sample; (b) annealed sample; and (c) hardened sample. Inverse pole figures (IPFs) obtained for direction Y (in the scanning plane) of the (d) as-printed sample; (e) annealed sample; and (f) hardened sample. IPFs obtained for direction Z (along building direction) of the (g) as-printed sample; (h) annealed sample; and (i) hardened sample. (For interpretation of the references to color in this figure legend, the reader is referred to the web version of this article.)

The defect in the top row of images was a cavity, whereas the defect in the bottom row of images was an unmelted particle that was embedded in the printed sample. At a plastic strain of about 1.5%, a crack first formed at the site of the lower defect (Fig. 18h). Subsequently, at a plastic strain of about 4%, a second crack was initiated at the site of the upper defect (Fig. 18b). The plastic deformation of the matrix surrounding the defects was evident. The cracks that originated at both defects initially propagated towards the edges of the sample (Fig. 18c and i). The fractures only began to propagate towards the other defect and through the entire body of the sample (Fig. 18f) following relatively large, localised plastic deformation (necking) in this region. The results also suggest that the skin (contour) layer of the printed sample was not a critical area for failure initiation.

4. Conclusions

A cellular microstructure with sub-μm-sized cells was observed in the as-printed maraging steel. The chemical composition of the cell boundaries slightly differed to that of the matrix. Numerous fine particles, as well as thin films consisting of retained austenite, were formed predominantly at the cell boundaries. The microstructure of the as-built sample possessed retained austenite with a volume fraction of 4%. The as-built samples had average tensile strength, total elongation, and hardness values of 1050 MPa, 8%, and 371 HV 0.1, respectively.
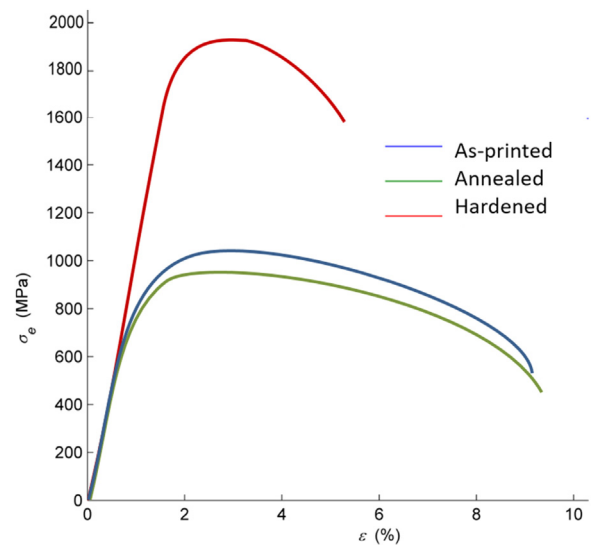

Fig. 15. Typical stress–strain curves obtained for the as-built (blue), solution-annealed (green), and precipitation-hardened (red) samples. (For interpretation of the references to color in this figure legend, the reader is referred to the web version of this article.)

Table 2
Mechanical properties of the additive-manufactured (AM) and conventional steels following identical heat treatments; the standard deviations are also listed.

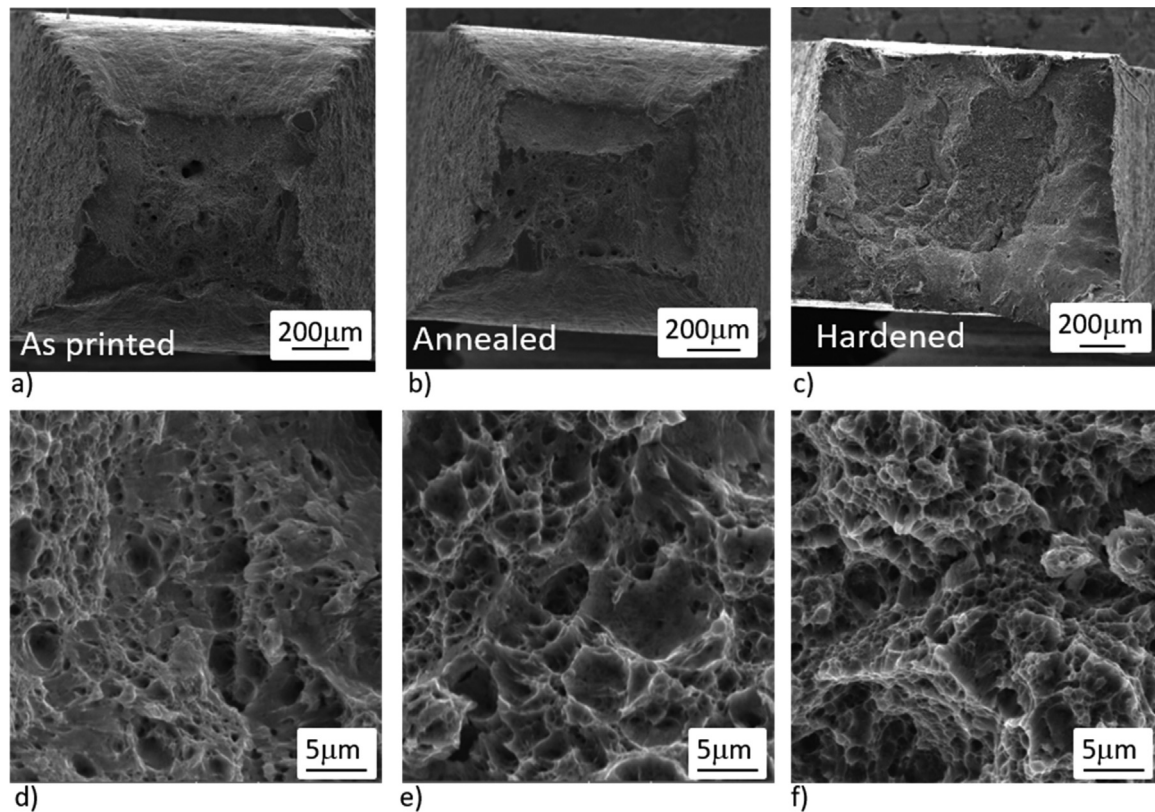|		ε [%]	σ	$Rp_{0.2}$ [MPa]	σ	Rm [MPa]	σ	HV 0.1	σ
No heat treatment	AM	8	1.2	903	98	1050	45	371	5
	Conventional	10	1.6	798	60	981	49	323	4
Solution-annealed	AM	9	0.4	799	87	980	34	328	7
	Conventional	11	0.5	770	62	930	66	339	7
Precipitation-hardened	AM	4	1.3	1641	104	1837	63	665	8
	Conventional	6	0.1	1645	56	1877	51	655	6

Fig. 16. SEM images of the fracture surfaces. The top row of images show general views of the (a) as-printed sample; (b) annealed sample; and (c) hardened sample. The second row shows detailed images of the (d) as-printed sample; (e) annealed sample; and (f) hardened sample.

The solution annealing resulted in the elimination of the cellular microstructure, and led to the complete transformation of the retained austenite, to martensite. The resultant tensile strength of the sample was slightly below 1000 MPa, which was accompanied by a total elongation value of 9% and hardness value of 328 HV 0.1. The precipitation hardening of the as-built samples resulted in partial dissolution of the cells. In addition, the austenite volume fraction increased to 8%. The hardness and tensile strength values of the hardened samples were over 1800 MPa and 665 HV 0.1, respectively. These values are almost double those obtained for the as-built samples.

The in-situ observation of the response of the as-built microstructure to the tensile loading highlighted the critical importance of the metallurgical purity of the AM products. The skin of the sample, which was printed using different parameters to those of the core, did not present any problems during straining. Fractures were initiated at two defects, namely an unmelted particle and a cavity.

Acknowledgements

Declarations of interest

None.

Author contributions

The experiments were designed and conceived by Ludmila Kučerová and Ivana Zetková. Ludmila Kučerová further analysed and evaluated the data and wrote the paper, and Ivana Zetkova was responsible for conducting the additive-manufacturing and post-treatment processes. Andrea Jandová performed the light microscopy and scanning electron
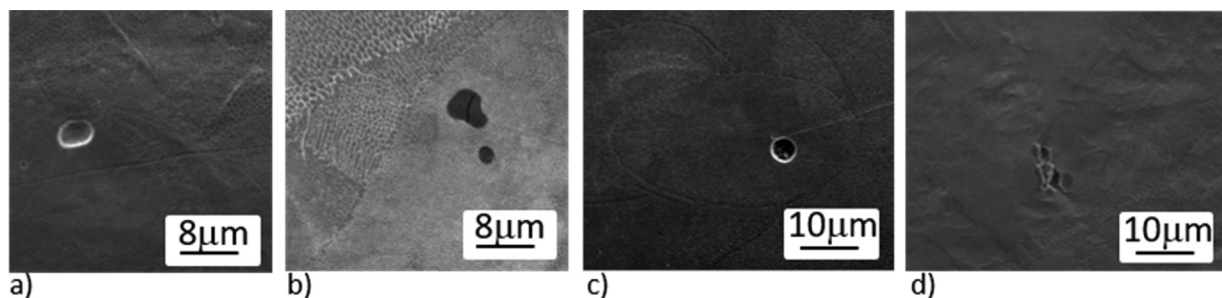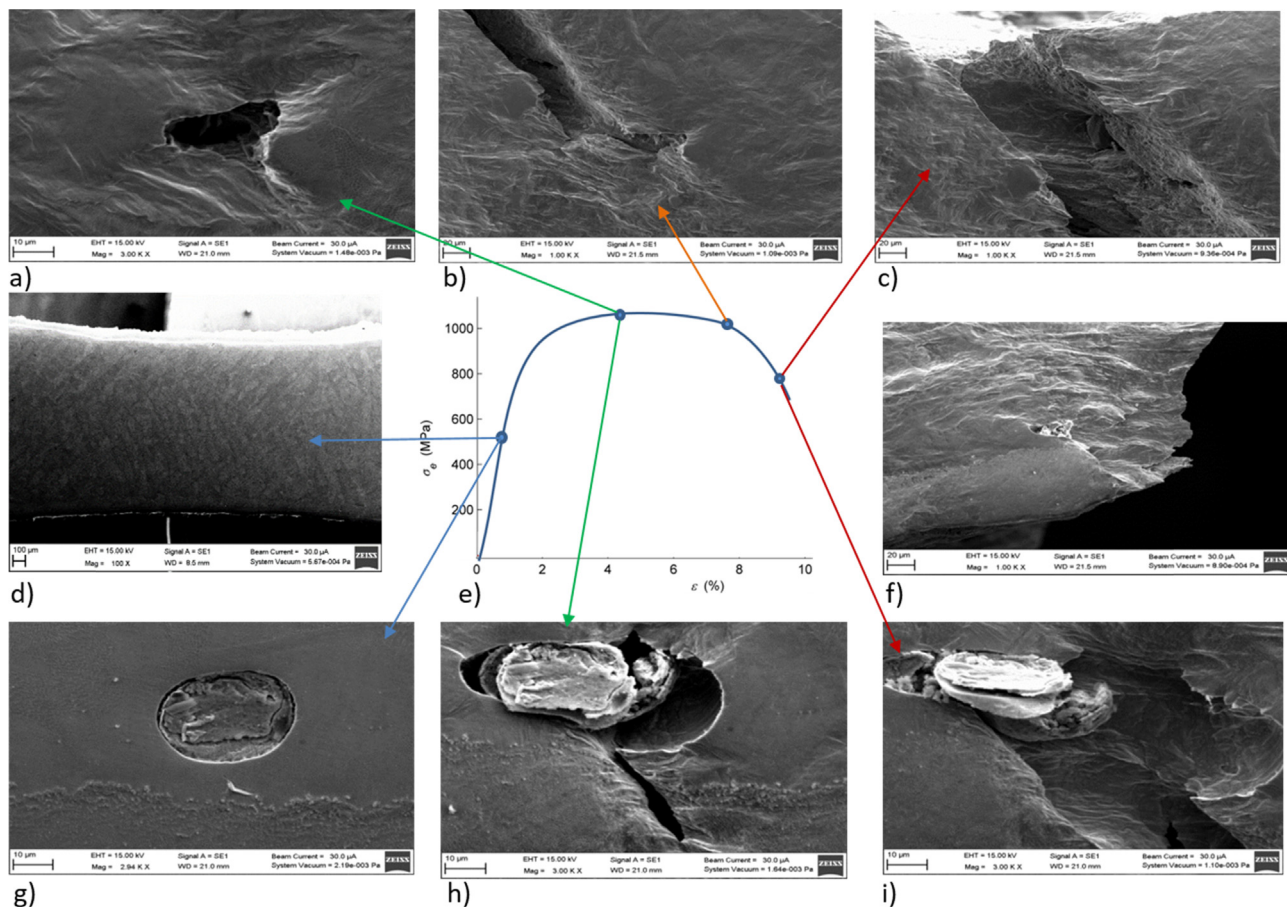

Fig. 17. Examples of defects found on the surface of the sample that were inspected prior to straining. (a) unmelted particle; (b) inclusion; (c) spherical cavity; (d) deformed and fragmented inclusion.

Fig. 18. Fracture initiation and propagation during tensile loading. Two defects (top and bottom rows of micrographs) led to failure initiation. Images showing the failure progression around (a, b, c) a cavity, and (g, h, i) an unmelted particle. Overview of (d) the etched sample surface prior to testing, and (f) the fracture surface. (e) Stress–strain diagram obtained during straining.

microscopy, and Martin Bystrianský conducted the mechanical testing and in-situ straining tests. All authors have approved the final article.

Data availability statement

The data required to reproduce these findings cannot be shared at this time because the data also forms part of an ongoing study.

References

[1] K. Kempen, E. Yasa, L. Thijs, et al., Microstructure and mechanical properties of selective laser melted 18Ni-300 steel, Phys. Procedia 12 (2011) 255–263, https://doi.org/10.1016/j.phpro.2011.03.033.

[2] H.W. Mindt, M. Megahed, N.P. Lavery, et al., Powder bed layer characteristics: the overseen first-order process input, Metall. Mater. Trans. A 47 (2016) 1–12, https://doi.org/10.1007/s11661-016-3470-2.

[3] H. Asgari, C. Baxter, K. Hosseinkhani, et al., On microstructure and mechanical properties of additively manufactured AlSi10Mg_200C using recycled powder, Mater. Sci. Eng. A 707 (2017) 148–158, https://doi.org/10.1016/j.msea.2017.09.041.

[4] Y. Bai, Y. Yang, D. Wang, et al., Influence mechanism of parameters process and mechanical properties evolution mechanism of maraging steel 300 by selective laser melting, Mater. Sci. Eng. A 703 (2017) 116–123, https://doi.org/10.1016/j.msea.2017.06.033.

[5] T.H. Simm, L. Sun, D.R. Galvin, et al., The effect of a two-stage heat-treatment on the microstructural and mechanical properties of a maraging steel, Materials 10 (2017) 1346, https://doi.org/10.3390/ma10121346.

[6] J. Mutua, S. Nakata, T. Onda, et al., Optimization of selective laser melting parameters and influence of post heat treatment on microstructure and mechanical properties of maraging steel, Mater. Des. 139 (2017) 486–497, https://doi.org/10.1016/j.matdes.2017.11.042.

[7] C.H. Tan, K. Zhoua, W. Ma, et al., Microstructural evolution, nanoprecipitation behavior and mechanical properties of selective laser melted high-performance grade 300 maraging steel, Mater. Des. 134 (2017) 23–34, https://doi.org/10.1016/j.matdes.2017.08.026.

[8] P. Kürnsteiner, M.B. Wilms, et al., A. Weisheit, In-process precipitation during laser additive manufacturing investigated by atom probe tomography, Microsc. Microanal. 23 (1) (2017) 694–695, https://doi.org/10.1017/S1431927617004135.

[9] L. Kučerová, I. Zetková, Metallography of 3D printed 1.2709 tool steel, Manuf. Technol. 16 (1) (2016) 140–144.

[10] P.R. Sakai, Comparison of mechanical and microstructural characteristics in maraging 300 steel welded by three different processes: LASER, PLASMA and TIG, Procedia Eng. 114 (2015) 291–297, https://doi.org/10.1016/j.proeng.2015.08.071.

[11] C.R. Shamantha, et al., Microstructural changes during welding and subsequent heat treatment of 18Ni (250-grade) maraging steel, Mater. Sci. Eng. A 287 (2000) 43–51, https://doi.org/10.1016/S0921-5093(00)00838-8.

[12] P.R. Sakai, D.F. da Silva, S. Lombardo, et al., Comparison of mechanical and microstructural characteristics in maraging 300 steel welded by PAW and GTAW processes submitted to repair, Adv. Mater. Res. 1135 (2016) 255–264, https://doi.org/10.4028/www.scientific.net/AMR.1135.255.

[13] J.A. Slotwinski, E.J. Garboczi, P.E. Stutzman, et al., Characterization of metal powders used for additive manufacturing, J. Res. Nat. Inst. Stand. Technol. 119 (2014) 460–493, https://doi.org/10.6028/jres.119.018.

[14] I. Zetková, L. Kučerová, M. Zetek, et al., Evaluation of metal powder for additive manufacturing of maraging steel, in: B. Katalinic (Ed.), Proceedings of the 28th DAAAM International Symposium; 20178-11, DAAAM International, Zadar, Croatia, 2007, pp. 410–416, , https://doi.org/10.2507/28th.daaam.proceedings.057.

[15] J.M.C. Azvedo, A.C. Serrenho, J.M. Allwood, The deformation of metal powder particles: hardness and microstructure, Procedia Eng. 207 (2017) 1200–1205, https://doi.org/10.1016/j.proeng.2017.10.870.

[16] A. Strondl, O. Lyckfeld, H. Brodin, et al., Characterization and control of powder properties for additive manufacturing, J. Miner. Met. Mater. Soc. 67 (2015) 549–554, https://doi.org/10.1007/s11837-015-1304-0.

[17] N. Clak, N. Jones, R. Setchi, et al., Particle size characterization of metals powders for additive manufacturing using a microwave sensor, Powder Technol. 327 (2018) 536–543, https://doi.org/10.1016/j.powtec.2017.11.042.

[18] E.A. Jägle, Z. Sheng, P. Kurnsteiner, et al., Comparison of maraging steel micro- and nanostructure produced conventionally and by laser additive manufacturing, Materials 10 (2017) 1–15, https://doi.org/10.3390/ma10010008.

[19] K. Monkova, I. Zetkova, L. Kučerová, et al., Study of 3D printing direction and effects of heat treatment on mechanical properties of MS1 maraging steel, Arch. Appl. Mech. (2018) 1–14, https://doi.org/10.1007/s00419-018-1389-3.